

# Polyelectrolyte Layer-by-Layer Deposition in Cylindrical Nanopores

Thomas D. Lazzara,<sup>§,†</sup> K. H. Aaron Lau,<sup>§,†,\*</sup> Ahmed I. Abou-Kandil,<sup>§</sup> Anne-Marie Caminade,<sup>||</sup> Jean-Pierre Majoral,<sup>||</sup> and Wolfgang Knoll<sup>§,‡</sup>

<sup>§</sup>Max Planck Institute for Polymer Research, Ackermannweg 10, D55128, Mainz, Germany, <sup>†</sup>Institute for Organic and Biomolecular Chemistry, Tamannstrasse 2, 37077, Göttingen, Germany, and <sup>||</sup>Laboratoire de Chimie de Coordination du CNRS, 205 route de Narbonne, F-31077, Toulouse cedex 04, France. <sup>‡</sup>Present address: Department of Biomedical Engineering, Northwestern University, 2145 Sheridan Road, Evanston, Illinois 60202. <sup>†</sup>Present address: Austrian Institute of Technology, Donau City Strasse 1, 1220 Vienna, Austria.

**L**ayer-by-Layer (LbL) assembly is a versatile technique to create multilayered structures by the alternating depositions of polycationic and polyanionic species. The technique has inherent advantages toward the nanoscale control of the layered material.<sup>1–7</sup> Multilayer formation is governed by electrostatic self-assembly of oppositely charged species and, therefore, as long as the LbL building blocks carry suitable charges, the size, structure, and nature of the building blocks can be modified to impart different functionalities to the LbL film. Technologically relevant functional films have been produced by the homogeneous or heterogeneous layered mixing of polyelectrolyte polymers<sup>8–11</sup> of various structures (linear, branched, dendritic, degree of hydrophobicity) and with different types of nanoparticles<sup>12–17</sup> and proteins.<sup>18,19</sup> A number of methods, such as X-ray diffraction, ellipsometry, and surface plasmon resonance, are now available to characterize planar LbL structures. However, advanced LbL structures formed inside porous systems, such as within films of colloidal particles or cylindrical nanoporous membranes,<sup>20–28</sup> cannot be easily characterized.

Nanoporous anodic aluminum oxide (AAO) films have been widely employed as versatile templates for the preparation of nanostructured functional materials.<sup>13,14,20–23,25,27,28</sup> It is a self-organized material that possesses nonintersecting, close-packed, cylindrical pores running straight through the film thickness. The pore diameters can be conveniently adjusted,<sup>24,29,30</sup> and the AAO can be prepared with minimum equipment requirements. Studies involving thin AAO films have attracted significant interest for their

**ABSTRACT** Layer-by-layer (LbL) deposition of polyelectrolytes within nanopores in terms of the pore size and the ionic strength was experimentally studied. Anodic aluminum oxide (AAO) membranes, which have aligned, cylindrical, nonintersecting pores, were used as a model nanoporous system. Furthermore, the AAO membranes were also employed as planar optical waveguides to enable *in situ* monitoring of the LbL process within the nanopores by optical waveguide spectroscopy (OWS). Structurally well-defined *N,N*-disubstituted hydrazine phosphorus-containing dendrimers of the fourth generation, with peripherally charged groups and diameters of approximately 7 nm, were used as the model polyelectrolytes. The pore diameter of the AAO was varied between 30–116 nm and the ionic strength was varied over 3 orders of magnitude. The dependence of the deposited layer thickness on ionic strength within the nanopores is found to be significantly stronger than LbL deposition on a planar surface. Furthermore, deposition within the nanopores can become inhibited even if the pore diameter is much larger than the diameter of the G4-polyelectrolyte, or if the screening length is insignificant relative to the dendrimer diameter at high ionic strengths. Our results will aid in the template preparation of polyelectrolyte multilayer nanotubes, and our experimental approach may be useful for investigating theories regarding the partitioning of nano-objects within nanopores where electrostatic interactions are dominant. Furthermore, we show that the enhanced ionic strength dependence of polyelectrolyte transport within the nanopores can be used to selectively deposit a LbL multilayer atop a nanoporous substrate.

**KEYWORDS:** porous substrates · cylindrical pores · polyelectrolytes · dendrimers · layer-by-layer self-assembly · optical lightmode waveguide spectroscopy

potential use in nondestructive, high sensitivity assays such as the selective separation of drug enantiomers<sup>31,32</sup> or DNA oligomers<sup>33</sup> and the development of on-chip biosensors<sup>34–37</sup> where miniaturization, device performance, and efficiency are required. Two dominant factors affecting macromolecular transport in the cylindrical geometry are steric effects and the electrostatic interactions with the pore surfaces.<sup>38</sup>

Dendrimers are macromolecules that typically have a spherical or globular shape originating from a regular 3-dimensional branching and have a highly defined molecular weight. Their compact size, uniformity and tunability are significant advantages for applications such as gene delivery agents, drug carriers and molecular sensors.<sup>39–42</sup>

\*Address correspondence to AaronLau@northwestern.edu.

Received for review April 12, 2010 and accepted May 31, 2010.

Published online June 16, 2010. 10.1021/nn1007594

© 2010 American Chemical Society

Polyelectrolyte dendrimers are dendritic structures with ionizable groups. In particular, water-soluble, globular *N,N*-disubstituted hydrazine phosphorus-containing dendrimers developed by Majoral and Caminade *et al.* have been extensively used to create functional multilayer LbL systems<sup>40</sup> such as sensor surfaces,<sup>43</sup> nanotubes,<sup>14,44</sup> capsules,<sup>45</sup> and energy-cascade sensor architectures.<sup>13</sup> Multilayers prepared from these polyelectrolyte dendrimers on a planar surface show a monotonic increase in layer thickness with the number of LbL deposition steps.<sup>43,45</sup> Additionally they have a lower degree of interlayer penetration than multilayers formed from linear polyelectrolytes because of their well-defined peripherally charged surface and their rigid internal hydrophobic structure.<sup>40,46</sup> Such structural properties make these dendrimers suitable model polyelectrolytes to study the LbL deposition process in nanoporous substrates.

The study of charged macromolecule and colloid transport within cylindrical pores has been of interest both on a theoretical<sup>38,47–53</sup> and a practical level.<sup>54,55</sup> Although diffusion through cylindrical pores for dilute systems of rigid neutral spheres is relatively well understood, this is not the case for systems of charged particles within charged nanopores. Comprehensive theoretical modeling of these systems is complex due to the electrostatic contributions and charge regulation in the confined nanopore geometry.<sup>52</sup> The partitioning of charged analytes inside and outside cylindrical pores is not simply described by changes in the Debye screening length ( $\lambda_{\text{Debye}}$ ) with changes in ionic strengths.<sup>48–51,53,56,57</sup> Calculations based on spherical charged particles and infinite cylindrical pores have shown that electrostatic interactions continue to significantly influence transport properties even at ionic strengths approaching 1 M and in cases where pore diameters are much larger than the size of the particles.<sup>49,53</sup> To facilitate the description of, respectively, the particle diameter ( $d$ ) relative to the pore diameter ( $D_0$ ) and relative to  $\lambda_{\text{Debye}}$ , the normalized parameters  $\alpha = d/D_0$  and  $\tau = D_0/2\lambda_{\text{Debye}}$  are often used.

A number of experimental studies have focused on measuring the apparent diffusion constants in nanoporous membranes,<sup>58,59</sup> and studies related to electroosmotic transport<sup>60,61</sup> and Coulter counters<sup>62–64</sup> have been previously reviewed. More recently, indirect measurement of the filling by polyelectrolyte multilayers of nanopores ranging from 100–500 nm has been carried out in the dried state by gas-flow porometry.<sup>65</sup> Nonetheless, direct investigation of surface processes occurring within nanoscale pores has been hampered by the limited availability of *in situ*, high-sensitivity, surface characterization techniques that can probe inside nanoporous morphologies.

Optical waveguide spectroscopy (OWS) is a highly sensitive yet experimentally simple technique for inde-

pendently characterizing the thickness and refractive index of optically transparent thin films.<sup>66,67</sup> In recent years, OWS has also been explored for *in situ* monitoring of processes occurring within AAO<sup>68–70</sup> and other nanoporous templates<sup>71–75</sup> at subnanometer sensitivities.<sup>68,69</sup> The nanoporosity ensures that scattering losses are minimal for optical waveguiding at visible or longer wavelengths, and that effective medium theory (EMT) can be applied to quantify processes occurring within the nanoporous AAO structure based on its refractive index responses.<sup>68,76,77</sup> In this regard, the ordered cylindrical pore morphology of AAO membranes lends itself to a simple EMT description using the Maxwell–Garnett approach.<sup>68,70,77</sup>

In this contribution, the LbL deposition of dendrimer polyelectrolytes within the nanopores of AAO was investigated by *in situ* OWS and EMT analysis, and the limiting conditions in terms of pore size and ionic strength were explored. The diameter of the AAO pores was varied between 30–116 nm, which corresponds to 4–17 times of the diameter of the dendrimers used (~7 nm).<sup>45,78–80</sup> The ionic strength was controlled by the addition of NaCl, with the lowest concentration set by the polyelectrolytes dissolved in ultrapure water, and the highest at 900 mM NaCl. In our experiments, LbL deposition within the nanopores occurred simultaneously on the internal pore surfaces and atop the AAO membrane on the planar surfaces between openings of the cylindrical nanopores. As proposed in earlier studies,<sup>68,70</sup> the depositions atop and within the AAO membrane were independently measured by OWS. Depositions on the AAO were compared with surface plasmon resonance (SPR) measurements of LbL deposition on a planar surface. In addition, *ex situ* scanning electron microscopy (SEM) was employed to corroborate the *in situ* OWS results. Electrostatic hindrance to LbL deposition of polyelectrolytes within a nanoporous structure is not unexpected. However, our results indicate that dependence of the deposited layer thickness on ionic strength within the nanopores is significantly stronger than deposition on a planar surface. In particular, LbL deposition can be completely inhibited within the nanopores even if the pore diameter was much larger than the diameter of the dendrimer polyelectrolyte, and increased ionic strengths were unable to compensate for this effect. Finally, the enhanced ionic strength effect was utilized to selectively deposit a polyelectrolyte multilayer atop the nanoporous AAO substrate.

## RESULTS AND DISCUSSION

**LbL Deposition within and atop Nanoporous AAO Membranes.** The structures of the polyelectrolyte dendrimers used, *N,N*-disubstituted hydrazine phosphorus containing dendrimers of the fourth generation (G4), are shown in Figure 1A. Each dendrimer has 96 peripheral charged groups, which are either all cationic or all anionic in

nature ( $G_4(+)$  =  $G_4(\text{NH}^+\text{Et}_2\text{Cl}^-)_{96}$ ,  $M_w = 32361$ ;  $G_4(-)$  =  $G_4(\text{CHCOO}^-\text{Na}^+)_{96}$ ,  $M_w = 35625$ ). At low ionic strengths, akin to unbranched polyelectrolytes, the counterions of most charged groups remain close to the dendrimers (counterion condensation) and the ionized groups are weakly screened. Since these groups are located on the periphery of the G4-polyelectrolyte, to minimize repulsive electrostatic interactions, the dendrimers adopt a moderately extended conformation commensurate with the dendrimer's symmetry. The theoretical diameter of the dendrimers in a fully extended conformation is  $\sim 10$  nm. At higher ionic strengths, enhanced overall charge screening allows an increase in the degree of dissociation and the diameter of the G4 dendrimers in solution has been measured to be  $\sim 7$  nm.<sup>45,79,80</sup>

G4-Polyelectrolyte LbL depositions were initiated on the nanoporous AAO membrane with an aminopropyl-dimethylethoxysilane (APDMES) surface layer that provided a positive surface charge. The AAO membranes were prepared with a thickness of  $\sim 1$   $\mu\text{m}$  and a range of average pore diameters ( $D_0$ ) of 30–117 nm. The pores are open only on the top side of the AAO membrane. On the APDMES-functionalized AAO substrates, LbL multilayer formation occurred *via* (1) deposition on the internal surface of the cylindrical pores and (2) deposition atop the nanoporous membrane on the surfaces between individual pore openings. G4-Polyelectrolyte depositions were performed starting from immersion in 1 mg/mL  $G_4(-)$  dissolved in ultrapure water solution, followed by immersion in a 1 mg/mL  $G_4(+)$  solution, and so forth, with a rinsing step in between every immersion. The ionic strength was controlled by the addition of NaCl.

As previously reported, the AAO membranes were prepared on glass substrates and the AAO also acted as optical waveguides.<sup>68,70,81</sup> This allowed *in situ* monitoring of the LbL deposition using optical waveguide spectroscopy (OWS).<sup>66</sup> In OWS, the intensity minima in reflectivity *versus* incidence angle measurements indicate conditions at which light is coupled through a prism into the AAO membrane (Figure 2). The deposited dendrimers have a higher dielectric constant ( $\epsilon_{\text{dendrimer}} = 2.25$ )<sup>45</sup> than the liquid they displace ( $\epsilon_{\text{water}} = 1.774$ ). Consequently, G4-polyelectrolyte deposition increases the overall dielectric constant inside the pores ( $\epsilon_{\text{pore}}$ ) and hence the dielectric constant of the entire AAO membrane waveguide ( $\epsilon_{\text{AAO}}$ ). Increases in  $\epsilon_{\text{AAO}}$  cause the waveguide mode minima to shift to higher angles.<sup>68,70,81</sup> Each deposition step was allowed to proceed until no further change was observed in the OWS signal (typically 30 min). Figure 3A shows the shifts in the waveguide mode minima for the transverse magnetic (TM) modes after successive LbL deposition steps on an AAO membrane ( $D_0 = 65$

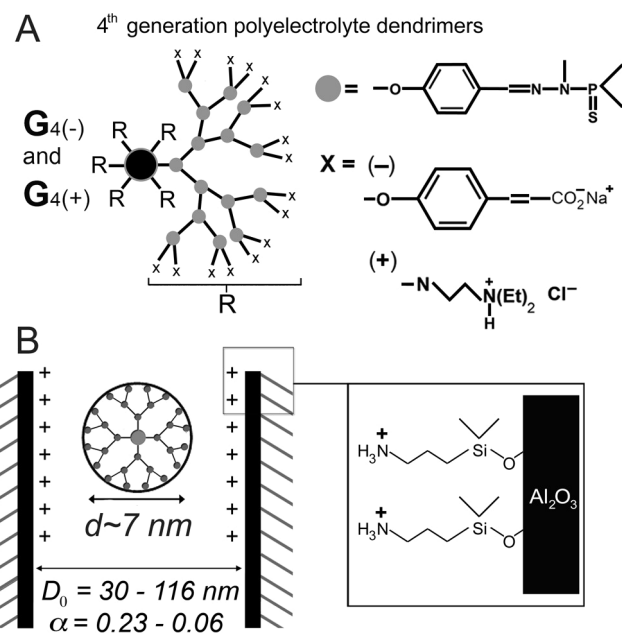
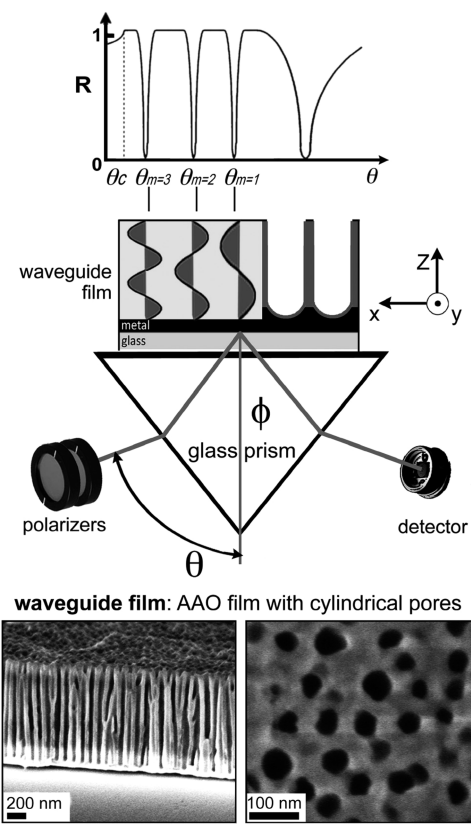


Figure 1. (A) Chemical structure of the *N,N*-disubstituted hydrazine phosphorus-containing dendrimers of the fourth generation (G4-polyelectrolyte) used in the LbL experiments. (B) Schematic illustrating the geometry of the polyelectrolyte multilayer experiments carried out within cylindrical nanopores of different diameters ( $D_0$ ), involving the interaction of charged dendrimers with a positively charged surface obtained by silanization with APDMES.

nm) using polyelectrolytes solutions with 100 mM NaCl.

Figure 3B shows the cumulative angle shifts of the TM mode minima after each LbL step for the experiment in 3A, and also that of a transverse electric (TE<sub>0</sub>) mode. It was observed that the cumulative angle shifts for all modes increased linearly up to five layers. However, the angle increase and deposition slowed thereafter, but at different rates for the different modes. Indeed, from the seventh layer on, the angle shifts for TE<sub>0</sub> became negligible, the TM<sub>1</sub> mode shifts became small, and only the TM<sub>2</sub> mode shifts were still obvious. In the waveguide, the electromagnetic fields of the different modes are distributed transversely in and around the AAO membrane with specific nodal patterns (Figure 2). In particular, higher order modes (e.g., TM<sub>2</sub> vs TM<sub>1</sub>) have larger fractions of their fields distributed toward the edges of the AAO membrane and are more sensitive to processes occurring atop the membrane.<sup>66</sup> Furthermore, TE modes have electric fields polarized in the plane of the membrane and are less sensitive than TM modes to processes atop the membrane. Deposition atop the pores contributes to increases in the AAO waveguide film thickness. Therefore, as discussed in previous reports,<sup>68,70</sup> the higher shifts of higher order modes (Figure 3) showed that LbL deposition atop the AAO proceeded continuously but that G4-polyelectrolyte deposition within the nanopores stopped after three bilayers.

The changes in  $\epsilon_{\text{AAO}}$  were derived from the angle changes in the waveguide modes using conventional

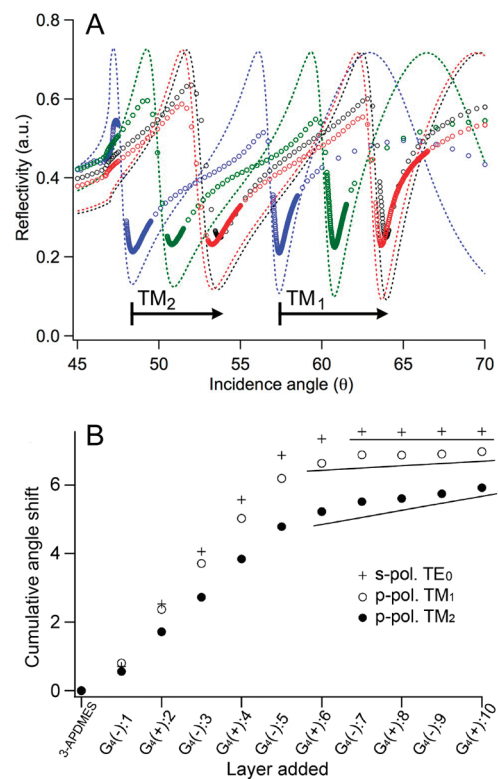


**Figure 2.** Schematic of the OWS setup used to measure waveguide modes, from which  $\epsilon_{\text{AAO}}$ ,  $t_{\text{in}}$  and  $t_{\text{atop}}$  were measured. The reflectivity ( $R$ ) is measured as a function of the incidence angle ( $\theta$ ). The idealized field distributions of several guided modes are shown. The excitation of these modes is detected as sharp minima in the  $R$  vs  $\theta$  measurements. Also shown are SEM images of the cross-section and the top view of an AAO waveguide membrane.

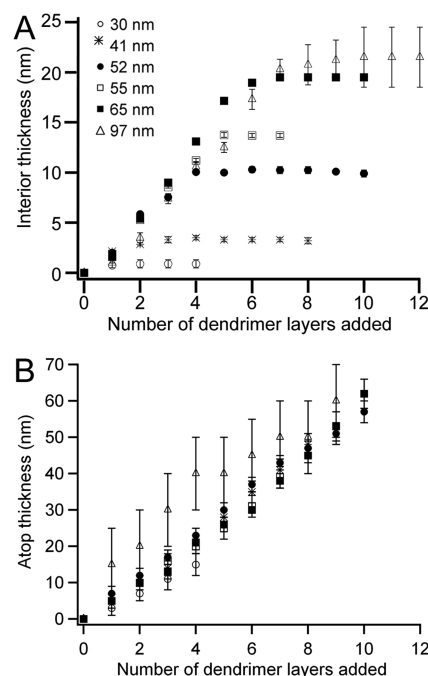
OWS Fresnel multilayer analysis,<sup>66</sup> and the thickness change on the interior pore surfaces ( $t_{\text{in}}$ ) was calculated from  $\epsilon_{\text{AAO}}$  using an effective medium theory (EMT)<sup>82</sup> model.<sup>68,70,81</sup> The atop thickness ( $t_{\text{atop}}$ ) was also obtained from Fresnel analysis that is constrained by an EMT calculated value of  $\epsilon_{\text{atop}}$  commensurate with the porosity indicated by  $\epsilon_{\text{AAO}}$  (Supporting Information, Figure S1). The thickness values obtained from both the OWS and EMT analyses are the averaged thicknesses of the polyelectrolyte layers, which have finite roughnesses.

Figure 4 shows both  $t_{\text{in}}$  and  $t_{\text{atop}}$  versus deposition steps ( $n$ ) of the G4-polyelectrolyte film deposited for membranes with a range of different pore diameters ( $D_0 = 30–97$  nm). This set of experiments was performed using dendrimer solutions with a moderate NaCl concentration of 100 mM. It is seen that  $t_{\text{in}}$  initially increased following a common linear trend regardless of the pore diameter, but then became inhibited (analogous to Figure 3) such that  $t_{\text{in}}$  ceased increasing beyond saturation values specific to each pore size.

In the initial linear regime, the average increase in  $t_{\text{in}}$  per polyelectrolyte layer ( $t_{\text{avg}}$ ) was 3.2 nm. This was



**Figure 3.** (A) Optical waveguide measurements (circles) with Fresnel calculations (----) for an APDMES-functionalized AAO waveguide with  $D_0 = 65$  nm in water and after 3, 6, and 9 G4-polyelectrolyte deposition steps from 100 mM NaCl solutions. The waveguide mode minima shift to higher angles as G4-polyelectrolytes deposit within and atop the pores. (B) The corresponding angle shifts of the minima of each TM mode and the TE<sub>0</sub> mode vs the number of LbL deposition steps.



**Figure 4.** Thicknesses of the G4-polyelectrolyte layers deposited from 100 mM NaCl aqueous solutions, within ( $t_{\text{in}}$ , A) and atop ( $t_{\text{atop}}$ , B) nanoporous AAO membranes with various pore diameters.

smaller than the native G4-polyelectrolyte diameter of  $\sim 7$  nm in solution.<sup>45,79,80</sup> In comparison, the thickness of a dried G4 dendrimer monolayer in air, measured by AFM, is  $\sim 2.5$  nm thick,<sup>79</sup> and the maximum thickness of our G4 layers measured on both a planar surface and within the pores is  $t_{\max} \approx 4.5$  nm (see discussion related to Figure 7);  $t_{\max}$  is consistent with the volume-averaged thickness (as measured by OWS or SPR) of a random sequentially adsorbed layer ( $\sim 55\%$  coverage)<sup>90</sup> of a  $\sim 7$  nm globular species, and one could relate the ratio  $t_{\text{avg}}/t_{\max} \approx 70\%$  to sub-monolayer coverage. However, the present optical techniques cannot independently measure surface coverage and the effects of surface-induced G4-polyelectrolyte compression and spreading, which is expected to contribute to the reduction in the layer thickness within the initial linear regime, as well as in subsequent deposition steps.

As expected,  $t_{\text{in}}$  saturation values were higher for larger pore diameters. However, the pores were far from being completely filled at these saturation values. For example, with  $D_0 = 65$  nm,  $t_{\text{in}}$  did not increase beyond 21.5 nm (after 6 LbL steps), while deposition within pores with  $D_0 = 30$  nm immediately reached saturation during the first deposition step.

Figure 4B shows the cumulative thickness of G4-polyelectrolytes deposited atop the AAO membrane on surfaces between the pores ( $t_{\text{atop}}$ ). Unlike  $t_{\text{in}}$ ,  $t_{\text{atop}}$  increased uninterrupted for all deposition steps for all  $D_0$  in a linear fashion. Furthermore, the rates of deposition for different  $D_0$  were essentially coincident with each other, which shows that  $t_{\text{atop}}$  was unaffected by the presence of the pores (deposition on the interpore surface proceeded with the same rate as on a flat surface).<sup>83</sup>

As pointed out above, the interior of the pores were not completely filled even after  $t_{\text{in}}$  reached saturation values. The pore diameter that remained "open" after successive LbL deposition steps (*i.e.*, open-pore diameter,  $D_{\text{open-pore}}$ ) may be estimated from  $D_{\text{open-pore}} = D_0 - 2t_{\text{in}}$ . For example, for  $D_0 = 65$  nm,  $t_{\text{in}} = 21.5$  nm, and  $D_{\text{open-pore}} = 22$  nm. (Note that  $t_{\text{in}}$  measured by OWS, and hence  $D_{\text{open-pore}}$ , is also the value averaged over the entire length of the pore ( $\sim 1$   $\mu\text{m}$ ), since the guided light in the OWS setup had a  $\lambda = 633$  nm and cannot resolve fine variations through the thickness of the AAO membrane).

The OWS data was also corroborated by *ex situ* scanning electron microscopy (SEM). Figure 5 shows that, after 10 deposition steps, the pores in the AAO membrane ( $D_0 = 65$  nm) were not completely filled ( $D_{\text{open-pore}} = 22$  nm). In the AAO cross-section image (Figure 5A) a layer of organic material can be observed on the pore walls. In the top view image (Figure 5B), most of the pores are observed to remain open (there is a distribution in the diameters of the pore openings in the AAO prepared, so the smaller pores appeared obscured). Exact values of  $t_{\text{in}}$  and

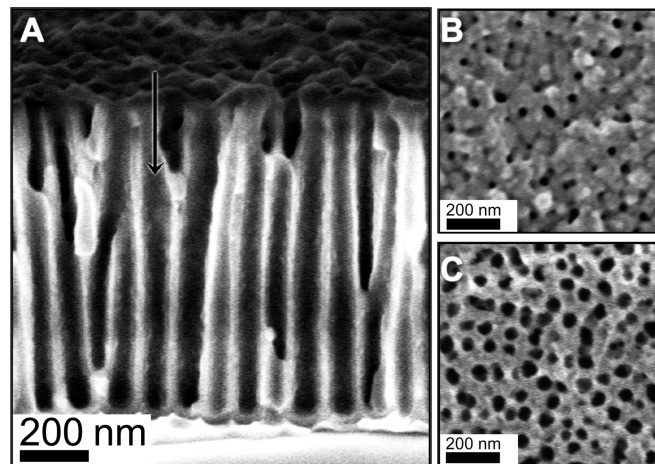
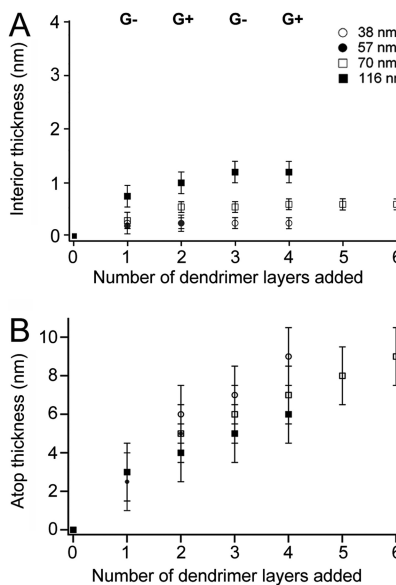


Figure 5. SEM images of (A) the interior and (B) atop the AAO membrane ( $D_0 = 65$  nm) after 10 deposition steps from 100 mM NaCl aqueous solution. (C) SEM image of the top surface of the AAO ( $D_0 = 70$  nm) after six deposition steps from ultrapure water solutions.

$D_{\text{open-pore}}$  may not be measured from SEM images as the vacuum environment in the SEM requires dried samples.<sup>79</sup>

The electrostatic screening length  $\lambda_{\text{Debye}}$  is  $< 1$  nm at the experimental NaCl concentration of 100 mM. Therefore, one might not have expected the deposition within the pores to be electrostatically hindered when  $D_{\text{open-pore}} = 22$  nm was significantly larger than  $d \approx 7$  nm,<sup>45,78–80</sup> the diameter of the G4-polyelectrolytes. However, as a polyelectrolyte dendrimer enters a nanopore similar in size to itself, due to charge regulation, the electrostatic potential around the polyelectrolyte is altered and the local ion concentration, hence the local screening length, may deviate from bulk values.<sup>52,59</sup> Furthermore, electrostatic repulsion arising from polyelectrolytes already deposited near pore entrances within the same deposition step can significantly hinder the transport of same-charge G4-polyelectrolytes further into the pores.

**Ionic Strength and Charge Effects on LbL Deposition within Nanopores.** At a low ionic strength, counterion condensation is dominant and only a fraction of the polyelectrolyte charged groups are dissociated.<sup>84–86</sup> G4-polyelectrolytes dissolved in ultrapure water corresponded to the minimum ionic strength possible in our experimental system. Under these conditions, transport into the pores was expected to be strongly hindered electrostatically due to large  $\lambda_{\text{Debye}}$  and Figure 6 shows that deposition of G4-polyelectrolyte dendrimer dissolved in ultrapure water within the pores was inhibited for all pore diameters  $D_0 = 30–116$  nm (Figure 6A). The cumulative layer thickness within the pores did not increase beyond  $\sim 1$  nm, regardless of the number of deposition steps. Concurrently, the deposition atop the AAO membrane (Figure 6B) proceeded in an approximately linear fashion with an average layer thickness of  $\sim 1.5$  nm per deposition step. Accordingly, Figure 5C ( $D_0 = 70$  nm) shows that the pore diameter



**Figure 6.** Thicknesses of the G4-polyelectrolyte layers deposited from ultrapure water solutions, within ( $t_{in}$ , A) and atop ( $t_{atop}$ , B) nanoporous AAO membranes with various pore diameters.

remained similar to the original value even after six deposition steps. Compared with the deposition at 100 mM NaCl,  $t_{atop}$  without added NaCl was significantly decreased. This decrease with lowering of ionic strength is consistent with LbL deposition on flat homogeneous substrates (see Supporting Information, Figure S2).

Increasing the ionic strength increases the degree of dissociation, and by increasing the NaCl concentration in our G4-polyelectrolyte solutions, we were able to increase the per layer dendrimer thickness on both flat surfaces and within the nanoporous AAO membranes. Higher ionic strengths also induce a denser polyelectrolyte surface packing due to a decrease in the electrostatic screening length, which suppresses repulsion between surface-bound dendrimers and those in solution. However, comparison between Figures 4 and 6 clearly shows that  $t_{in}$  was more strongly hindered than  $t_{atop}$  by the electrostatic interactions such that (1) G4-polyelectrolyte deposition within the pores was inhibited at low ionic strength for all  $D_0$  tested, and (2) G4-polyelectrolyte per layer thickness was lower within than atop the pores even at 100 mM NaCl.

We further investigated the ionic strength effect by measuring the G4-polyelectrolyte layer thickness over a range of NaCl concentrations (0–900 mM). In Figure 7, the thickness of the initial G4 layer within the pores is plotted, and AAO samples with  $D_0 = 35$  and 54 nm were compared with the deposition on a flat surface (measured by SPR). We observed that the G4-polyelectrolyte single layer thickness increased to a

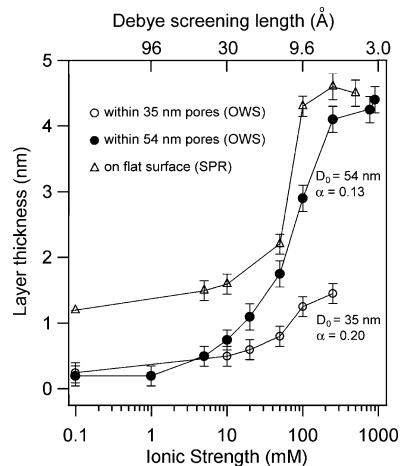


**Figure 7.** Initial G4-polyelectrolyte layer thickness deposited within AAO pores at increasing NaCl concentrations, in cylindrical pores  $D_0 = 35$  and 54 nm (measured by OWS), and on a flat surface (measured by SPR) (see Supporting Information, Figure S5 for the data presented using a linear scale).

maximum of 1.2 nm within the smaller 35 nm pores, and to a maximum of 4.5 nm within both the larger 54 nm pores and on the flat surface. However, to obtain a G4-polyelectrolyte layer thickness within the 54 nm pores similar to that on the flat surface, greater salt concentrations were required. At the same time, at high NaCl concentrations, only a third of the thickness was deposited within the 35 nm pores as compared to within the 55 nm pores. Indeed, the differences between the thicknesses measured on the flat surface and within the pores represent the effect of the cylindrical nanoporous geometry on G4-polyelectrolyte deposition as a function of the pore diameter. This effect is not limited to dendrimer polyelectrolytes. Roy *et al.* have performed similar experiments with linear PAH/PSS polyelectrolytes in 100 mM acetate buffer showing that the layer thickness within the pores of track-etched polycarbonate membranes (100, 200, and 500 nm pore diameters) was increased 2–4 times if the ionic strength was increased by an additional 0.5 M NaCl.<sup>65</sup>

We examined in more detail the electrostatic nature of the enhanced hindrance to polyelectrolyte dendrimer transport that results in a large  $D_{open-pore}$  to G4-polyelectrolyte diameter ratio. Figure 8A highlights the three regimes observed for the interior layer thickness ( $t_{in}$ ) versus the number of deposition steps ( $n$ ): (1) initial linear LbL deposition, (2) a transition regime, and (3) complete inhibition of the LbL process within the pores. As discussed earlier, the repulsive potential surrounding pore entrances created by the initial deposition of G4-polyelectrolytes and subsequent charge inversion in these locations likely contributed to the eventual inhibition of further deposition within the nanopores. Therefore a distribution in the size of the pore entrances would contribute to the transition regime, since the smaller entrances would be inhibited first. Additionally, since the OWS measurement of  $t_{in}$  represents a value

averaged over the entire length of the AAO pore, the transition regime (2) could also indicate a gradual build-up of an electrostatic barrier surrounding the pore entrances that localized the deposition more and more toward the pore openings. In this case, the number of polyelectrolyte layers deposited near the pore openings may be more accurately described by the total number of deposition steps in regimes (1) and (2) before the deposition became completely inhibited ( $n_{\max}$ , Figure 8B). Applying this assumption to calculating the *local* open-pore diameter near the pore entrances ( $D_{\text{local}}$ ) yields:

$$D_{\text{local}} = D_0 - 2n_{\max}t_{\text{avg}} \quad (1)$$

where  $t_{\text{avg}}$  is the average layer thickness within the linear regime eq 1.

Figure 8C plots  $D_{\text{local}}$  against the original pore diameter  $D_0$  for the experiments performed at 100 mM NaCl. It is seen that  $D_{\text{local}}$  does not depend on  $D_0$ , and the pores became inhibited at an average  $D_{\text{local}} \approx 26$  nm. Taken at face value, this represents a G4-polyelectrolyte diameter to screening length ratio  $\tau_{\text{local}} = D_{\text{local}}/2\lambda_{\text{Debye}} \approx 14$ , which is much larger than conventionally assumed ( $\lambda_{\text{Debye}}$  being interpreted as the length over which electrostatic interactions are screened to 1/e of its full strength).

Typically, in neutral-charge systems, when  $D_{\text{open-pore}}$  is comparable to the diameter of a transported object ( $d$ ) (i.e., large  $\alpha = d/D_{\text{open-pore}} \rightarrow 1$ ), the partitioning ( $\Phi$ ) within cylindrical pores becomes sterically limited according to  $\Phi = (1 - \alpha)^2$  (Figure 8D).<sup>59</sup> Therefore, in the absence of electrostatic interactions, as the limit  $\alpha \rightarrow 1$  is approached, dendrimer diffusion into nanopores would already become hindered. In the case of G4-polyelectrolytes, after initial dendrimer deposition around the pore entrances, the repulsive potential that is built up around the pore entrances causes the partitioning of the G4-polyelectrolyte to be even more strongly inhibited than the  $(1 - \alpha)^2$  steric limit (Figure 8D). Hence dendrimer partitioning and LbL deposition within a nanopore are strongly dependent on the electrostatic conditions and may already become negligible at  $0 < \alpha \ll 1$ . In fact, our data indicate a limiting value of  $\alpha_{\text{limit}} = d/D_{\text{local}} = 0.27$  for G4-polyelectrolyte at 100 mM NaCl. When the NaCl concentration was halved (50 mM), we measured  $D_{\text{local}} = 38$  nm and  $\alpha_{\text{limit}}$  decreased to 0.18 (Figure S3). A qualitatively similar behavior is observed in experiments involving linear polyelectrolyte multilayers in track-etched polycarbonate membranes (100 nm diameter pores).<sup>65</sup>

If the polyelectrolytes were to be deposited deeper within the pore, the remaining pore entrance ( $D_{\text{local}}$ ) must accommodate both the diameter of the diffusing G4-polyelectrolytes and the electrostatic double layers associated with both the diffusing and surface-bound polyelectrolytes. This criterion may be expressed, as a

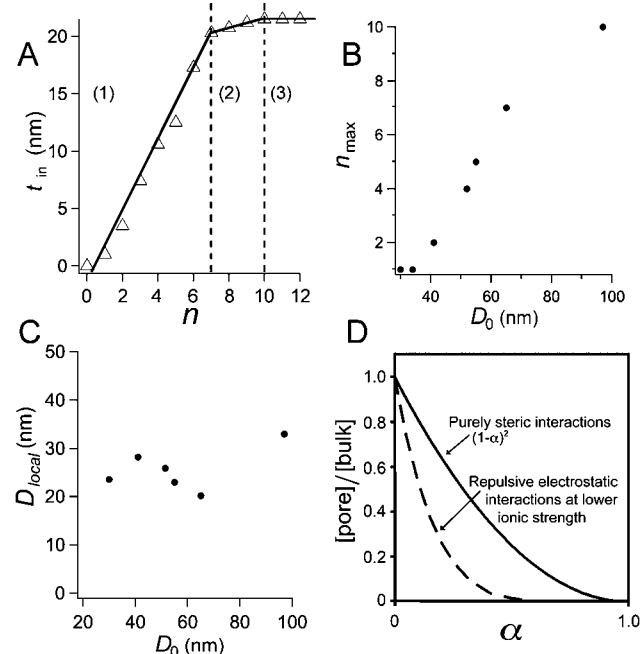


Figure 8. (A) Dendrimer deposition within  $D_0 = 97$  nm pores from a 100 mM NaCl solution. Three regimes are defined: (1) linear increase with additional deposition steps ( $n$ ); (2) a transition exhibiting hindered LbL deposition; and (3) inhibited LbL deposition due to electrostatic effects in a confined geometry. (B) Replot of the data shown in Figure 4A in terms of the maximum number ( $n_{\max}$ ) of dendrimer layers deposited: regimes 1 + 2 vs  $D_0$ . (C)  $D_{\text{local}}$  calculated from the data shown in Figure 4A using eq 1. (D) The partitioning of a charged particle inside cylindrical pores as a function of the relative particle diameter  $\alpha = d/D_0$ . Adapted with permission from ref 57. Copyright 1983 Elsevier.

first approximation, as one examines the AAO pore geometry:

$$D_{\text{local}} = d + 4\lambda_{\text{local}} \quad (2)$$

where  $\lambda_{\text{local}}$  is the screening length locally modified in the pores due to charge regulation, and it is assumed that the local screening length is identical over the G4-polyelectrolyte in solution and on the polyelectrolyte-covered pore surfaces. Accordingly, given  $D_{\text{local}} = 26$  nm at 100 mM NaCl in the bulk solution,  $\lambda_{\text{local}} = 4.75$  nm. This local value is much larger than the bulk  $\lambda_{\text{Debye}} = 0.96$  nm, which may explain the very large limiting values of  $D_{\text{local}}$  and  $\tau_{\text{local}}$  measured experimentally, and highlights the considerations of charge regulation and pore geometry (localized polyelectrolyte and counterion partitioning) that apply to LbL deposition within nanoporous systems.

#### Selective Formation of Polyelectrolyte Membranes atop AAO.

A polyelectrolyte membrane may be selectively formed atop the AAO membrane while maintaining negligible deposition within the pores, by taking advantage of the hindered polyelectrolyte deposition within the pore at a low ionic strength, and promoting the deposition of G4-polyelectrolytes atop the AAO pores. To begin, G4-polyelectrolytes LbL deposition was carried out with solutions of the dendrimers dissolved in ultrapure water.

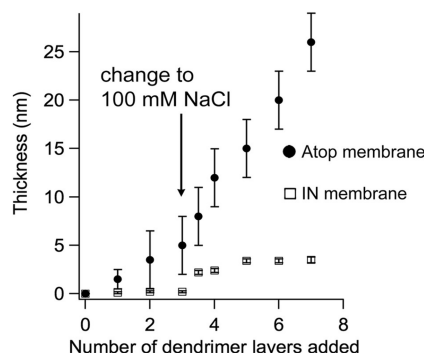


**Figure 9.**  $t_{\text{atop}}$  (circles) and  $t_{\text{in}}$  (squares) obtained by a 2-step protocol for selectively depositing a polyelectrolyte membrane atop empty pores: Deposition of G4-polyelectrolytes first from an ultrapure water solution (layers 1–3), followed by deposition from a solution with 100 mM NaCl. As the salt concentration was increased after the deposition of layer 3 from a solution of G4(–) dissolved in pure water, the LbL film thickness increased and is indicated as layer 3<sup>1/2</sup>.

This was followed by LbL deposition of G4-polyelectrolytes dissolved in 100 mM NaCl or higher ionic strengths. As discussed, the low salt condition of the first deposition stage prevented deposition within the pores and promoted deposition around the pore openings on the top of the AAO membrane. This first deposition stage effectively narrowed the diameter near the pore openings and inhibited the deposition of additional polyelectrolyte material within the pores, even at high bulk ionic strengths, in the second stage.

Figure 9 shows the evolution of the inner and atop dendrimer film thickness for an AAO membrane with  $D_0 = 55$  nm, for a deposition sequence beginning with ultrapure water solutions (three layers), followed by a second-stage deposition with G4-polyelectrolyte dissolved in solutions with 100 mM NaCl. At the end of the first deposition stage, it was observed that the pores remained essentially empty while the atop thickness grew to an average of ~5 nm per layer. After the NaCl concentration was increased in the second stage, the slope of the atop deposition curve increased and the atop thickness reached 26 nm at the end of the seventh step. In contrast, the layer thickness increase within the pores in the second high-salt deposition stage was minimal and quickly reached a saturation value. In comparison, an interior thickness of ~15 nm would be obtained in conventional one-stage deposition at 100 mM NaCl for the same  $D_0$  (see Figure 4).

The deposition atop the AAO was observed to vary proportionally with the ionic strength and a thick multilayer film could also be deposited this way. Polyelectrolyte membranes have been prepared above porous substrates for applications in nanofiltration and separation applications,<sup>87</sup> and also for other practical applications such as gas and chemical separation. The presented method is a simple and effective way to produce pore-spanning multilayer membranes and combines

the advantageous properties of multicomponent polyelectrolyte based membranes and permeable porous AAO solid supports.

## CONCLUSION

The effects of pore size and ionic strength on the layer-by-layer (LbL) deposition of polyelectrolyte dendrimers within the cylindrical nanopores of anodic aluminum oxide (AAO) membranes were experimentally studied *in situ* by optical waveguide spectroscopy (OWS). The OWS results were corroborated by *ex situ* SEM characterization, and were also compared to regular LbL deposition on a planar surface characterized by surface plasmon resonance spectroscopy (SPR). Globular *N,N*-disubstituted hydrazine phosphorus containing dendrimer polyelectrolytes of the fourth generation (G4-polyelectrolyte) were used as the model deposition species. It was demonstrated that OWS could independently quantify the thickness of the LbL deposited layers within, and atop, the AAO membrane with high sensitivity.

The deposition atop the AAO on surfaces between the pore openings was observed to follow the behavior of linear LbL deposition on a regular planar surface. However, LbL deposition within the cylindrical nanopores, after an initial linear deposition regime, became completely inhibited when the pores were still significantly larger than the diameter of the G4-polyelectrolyte (~7 nm). In fact, the interior deposition could be inhibited at all pore diameters investigated ( $D_0 = 30$ –116 nm) by adjusting the ionic strength of the deposition solution *via* the NaCl concentration. Conversely, a significant increase in the solution ionic strength, much greater than indicated by experiments on flat surfaces, was required to efficiently load the polyelectrolytes within the nanopores. Partitioning of dendrimers within the nanopores was already expected to be sterically hindered. Additionally, as LbL deposition initially occurred near the pore entrances before proceeding further within the pore, the initial charge inversion in the vicinity of the pore entrances likely created a repulsive potential that further inhibited partitioning of polyelectrolytes in the pores. For example, at 100 mM NaCl, we measured a limiting G4-polyelectrolyte to pore diameter ratio  $\alpha_{\text{limit}} = 0.27$ , while halving the NaCl concentration decreased  $\alpha_{\text{limit}}$  to 0.18.

Numerous applications, including separation and controlled drug release, gene delivery, analyte trapping, chemical catalysis within cavities, as well as sensor devices, have been suggested for LbL multilayered nanotubes,<sup>14,31–33,44</sup> and our results set useful parameters for their preparation using the strategy of nanoporous template fabrication. The present experimental approach of *in situ* OWS characterization of the AAO system may also be useful for investigating theories

describing the transport of charged macromolecules in charged pores. Finally, by manipulating the sequence of LbL deposition at different ionic strengths, a 2-step method was demonstrated to selectively deposit multi-layer polyelectrolyte films atop AAO membranes with

negligible interior deposition. Such differentiated substrates could have applications in which the compartmentalization of the contents between, or the differential functionalization of, the interior and exterior of a nanoporous membrane are required.

## EXPERIMENTAL SECTION

**Materials.** Fourth generation *N,N*-disubstituted hydrazine phosphorus-containing dendrimers having 96 charged terminal groups were synthesized according to a previously reported protocol.<sup>40,88</sup> High purity 11-mercaptopentadecanoic acid (MUA) and 3-aminopropyltrimethoxysilane (APDMES) were purchased from Sigma-Aldrich and used as received. Oxalic acid, phosphoric acid, toluene, and ethanol were of ACS reagent grade. Ultrapure deionized water (resistivity = 18.2 MΩcm) was obtained from a Millipore filtration machine (Millipore, Schwabach, Germany). High refractive index LaSFN9 glass substrates ( $\epsilon = 3.406$  at 632.8 nm) were obtained from Hellma Optik (Halle, Germany). 99.999% Al disks (20 mm × 1 mm) were purchased from Goodfellow (Bad Nauheim, Germany). The optical adhesive used (NOA 83H) was purchased from Norland Products (Cranbury, USA).

**AAO Waveguide Membranes.** (Figure 2). AAO membranes were prepared by two different protocols depending on the desired pore diameter. Membranes with pore diameters  $<75$  nm and lattice spacing = 100 nm were prepared by anodization of 1 μm sputtered Al films in 0.3 M oxalic acid at 40 V with a 25 nm thick Al layer left unanodized between the AAO membrane and the glass substrate for optical coupling, according to a previously reported method.<sup>70</sup> For AAO membranes with  $D_0 > 75$  and 175 nm lattice spacing, 1.5 μm AAO anodized from bulk Al discs were mounted on LaSFN9 glass slides using an optical adhesive according to another previously reported technique.<sup>81</sup> The Al discs were anodized in 0.05 M oxalic acid at 80 V for 20 min. The pores for all AAO membranes were widened to the desired diameter by etching in 5 wt % phosphoric acid (etch rate = 0.3 nm/min). Furthermore, all AAO membranes were functionalized with APDMES via solution silanization by refluxing for 12–15 h in a 2 vol % APDMES solution in toluene.<sup>84</sup>

**Surface Plasmon Resonance (SPR).** SPR measurements were performed on a purpose-built setup operating at 632.8 nm in the Kretschmann configuration.<sup>66</sup> LASFN9 glass substrates coated with 2 nm Cr and 50 nm Au (by thermal evaporation using an Auto300, BOC Edwards, U.K.) were used. The Au-coated substrates were functionalized with MUA self-assembled monolayers by immersion in 5 mM MUA in ethanol for 3 h followed by copious rinsing with ethanol.

**Optical Waveguide Spectroscopy (OWS).** OWS measurements of the AAO membranes prepared on glass slides were performed using the same setup as that used for SPR.<sup>66</sup> The glass-side of an AAO sample was attached to the base of a symmetric LaSFN9 glass prism by optical immersion oil. The laser ( $\lambda = 632.8$  nm) was incident through the prism-substrate assembly and reflected off the thin metal coupling layer in between the AAO membrane and the glass substrate as the incidence angle ( $\theta$ ) was varied. At specific  $\theta$  values determined by the thickness and the dielectric constant of the AAO membrane ( $\epsilon_{AAO}$ ), the laser was coupled into the membrane, and such waveguide modes were measured as sharp minima in a reflectivity ( $R$ ) vs  $\theta$  scan (Figure 2). Transverse electric (TE) and transverse magnetic (TM) modes were indexed according to the number of nodes in their electromagnetic field distributions.<sup>66</sup>  $\epsilon_{AAO}$  and the thickness of the AAO film, as well as any overlayers on top of the AAO, were calculated from the angles of the waveguide mode reflectivity minima using Fresnel equations, which exactly describe the layered geometry of the AAO waveguide in the OWS setup;<sup>66,89</sup> tracking the coupling angle of a mode enabled real time, *in situ* monitoring of changes in the thickness or the dielectric constant of the film.<sup>66</sup>

**Effective Medium Theory Analysis.** The  $\epsilon_{AAO}$  measured by OWS includes contributions from both the alumina, the medium filling

the pores (e.g., water), and any organic thin layer coating the pore surfaces (i.e., the G4 polyelectrolyte). Because of the anisotropic nature of the long, cylindrical AAO pores,  $\epsilon_{AAO}$  also has an anisotropic component that is described by the infinite, prolate ellipsoid approximation within the Maxwell–Garnett theory.<sup>76,77</sup>

$$\epsilon_{AAO}^{\perp} = \epsilon_{alumina} + f_{pore}(\epsilon_{pore} - \epsilon_{alumina}) \quad (2A)$$

$$\epsilon_{AAO}^{\parallel} = \epsilon_{alumina} \frac{\epsilon_{alumina} + \frac{1}{2}(1 + f_{pore})(\epsilon_{pore} - \epsilon_{alumina})}{\epsilon_{alumina} + \frac{1}{2}(1 - f_{pore})(\epsilon_{pore} - \epsilon_{alumina})} \quad (2B)$$

where  $\epsilon_{AAO}^{\perp}$  and  $\epsilon_{AAO}^{\parallel}$  are, respectively, the effective dielectric constant components normal and parallel to the AAO membrane surface,  $f_{pore}$  is the pore volume fraction within the AAO,  $\epsilon_{alumina} = 2.68^{70}$  is the dielectric constant of bulk anodic alumina at  $\lambda = 632.8$  nm, and  $\epsilon_{pore}$  is the (effective) dielectric constant within the pores. For a blank AAO film in water,  $\epsilon_{pore} = \epsilon_{water} = 1.77$ . With the addition of an organic film,  $\epsilon_{organic} = 2.25^{45}$  on the internal pore surfaces (e.g., APDMES or G4-polyelectrolyte), the volume within the pores would be occupied by a combination of the organic material and the pore filling medium.  $\epsilon_{pore}$  was then approximated by recursively applying eq 2 to the pore-organic film geometry:<sup>68,69</sup>

$$\epsilon_{pore}^{\perp} = \epsilon_{water} + f_{organic}(\epsilon_{organic} - \epsilon_{water}) \quad (3A)$$

$$\epsilon_{pore}^{\parallel} = \epsilon_{water} \frac{\epsilon_{water} + \frac{1}{2}(1 + f_{organic})(\epsilon_{organic} - \epsilon_{water})}{\epsilon_{water} + \frac{1}{2}(1 - f_{organic})(\epsilon_{organic} - \epsilon_{water})} \quad (3B)$$

where  $f_{organic}$  is the volume fraction of the organic layer within the cylindrical pores and the organic layer thickness ( $d_{organic}$ ) could then be calculated from  $f_{organic}$  and the pore diameter by assuming that the organic film formed a conformal layer on the pore surfaces:

$$d_{organic} = \frac{D_{pore}}{2}(1 - \sqrt{1 - f_{organic}}) \quad (4)$$

**Scanning Electron Microscopy (SEM).** SEM measurements were performed with a LEO Gemini 1530 SEM with acceleration voltages between 1 and 6 kV.

**Polyelectrolyte Dendrimer Deposition.** G4 polyelectrolyte concentrations were all 1 mg/mL, dissolved in ultrapure water. Different ionic strengths were obtained by directly adding microliter aliquots of a 1 or 10 M NaCl stock solution to the prepared solutions. After four deposited layers, newly prepared dendrimer solutions were used to ensure that the polyelectrolyte concentration remained constant. The G4-polyelectrolytes were deposited by flowing the solutions through a liquid flow cell, until saturation was reached in the recorded signal (between 15 and 45 min). The samples were all rinsed with ultrapure water before measuring the  $R$  vs  $\theta$  waveguide spectra. A flow rate of 0.4 mL/min was used, and the flow cell consisted of a 1 mm thick PDMS stamp with an  $8 \times 4$  mm rectangular opening. At near zero ionic strength, the interior deposition is negligible, and all experiments without added salt were only carried out for a maximum of six deposited layers.

**Acknowledgment.** T. D. Lazzara acknowledges the award of a doctoral scholarship from *Les Fonds Québécois de Recherche sur la Nature et les Technologies*. We thank Gunnar Glasser at the MPI

for Polymer Research for electron microscopy. We also thank Stefan Schmidt and Dr. Peter Detemple at the Institut für Mikrotechnik Mainz for providing Al thin film deposition services.

*Supporting Information Available:* SPR data of LbL dendrimer multilayer formation on flat surfaces; OWS data for depositions at other NaCl concentrations; SEM images of a multilayer film atop the pores and corresponding OWS data; layer model used for Fresnel calculations; and the measured overall dielectric constants of the porous alumina–polyelectrolyte structure are presented. This material is available free of charge via the Internet at <http://pubs.acs.org>.

## REFERENCES AND NOTES

1. Decher, G.; Schlenoff, J. B. *Multilayer Thin Films: Sequential Assembly of Nanocomposite Materials*. Wiley-VHC: Weinheim, Germany, 2003.
2. Bertrand, P.; Jonas, A.; Laschewsky, A.; Legras, R. Ultrathin Polymer Coatings by Complexation of Polyelectrolytes at Interfaces: Suitable Materials, Structure and Properties. *Macromol. Rapid Commun.* **2000**, *21*, 319–348.
3. De Geest, B. G.; Sanders, N. N.; Sukhorukov, G. B.; Demeester, J.; De Smedt, S. C. Release Mechanisms for Polyelectrolyte Capsules. *Chem. Soc. Rev.* **2007**, *36*, 636–649.
4. Decher, G. Fuzzy Nanoassemblies: Toward Layered Polymeric Multicomposites. *Science* **1997**, *277*, 1232–1237.
5. Decher, G.; Hong, J. D.; Schmitt, J., III. Consecutively Alternating Adsorption of Anionic and Cationic Polyelectrolytes on Charged Surfaces. *Thin Solid Films* **1992**, *210*, 831–835.
6. Iler, R. K. Multilayers of Colloidal Particles. *J. Colloid Interface Sci.* **1966**, *21*, 569–594.
7. Joanny, J. F. Polyelectrolyte Adsorption and Charge Inversion. *Eur. Phys. J. B* **1999**, *9*, 117–122.
8. Anzai, J.; Kobayashi, Y.; Nakamura, N.; Nishimura, M.; Hoshi, T. Layer-by-Layer Construction of Multilayer Thin Films Composed of Avidin and Biotin-Labeled Poly(amine)s. *Langmuir* **1999**, *15*, 221–226.
9. Caruso, F.; Caruso, R. A.; Mohwald, H. Production of Hollow Microspheres from Nanostructured Composite Particles. *Chem. Mater.* **1999**, *11*, 3309–3314.
10. Dobrynin, A. V.; Rubinstein, M. Theory of Polyelectrolytes in Solutions and at Surfaces. *Prog. Polym. Sci.* **2005**, *30*, 1049–1118.
11. Hammond, P. T. Form and Function in Multilayer Assembly: New Applications at the Nanoscale. *Adv. Mater.* **2004**, *16*, 1271–1293.
12. Fendler, J. H. Self-Assembled Nanostructured Materials. *Chem. Mater.* **1996**, *8*, 1616–1624.
13. Feng, C. L.; Zhong, X. H.; Steinhart, M.; Caminade, A. M.; Majoral, J. P.; Knoll, W. Graded-Bandgap Quantum-Dot-Modified Nanotubes: A Sensitive Biosensor for Enhanced Detection of DNA Hybridization. *Adv. Mater.* **2007**, *19*, 1933–1936.
14. Kim, D. H.; Karan, P.; Goring, P.; Leclaire, J.; Caminade, A. M.; Majoral, J. P.; Gosele, U.; Steinhart, M.; Knoll, W. Formation of Dendrimer Nanotubes by Layer-by-Layer Deposition. *Small* **2005**, *1*, 99–102.
15. Liu, Y. J.; Wang, Y. X.; Claus, R. O. Layer-by-Layer Ionic Self-Assembly of Au Colloids into Multilayer Thin-Films with Bulk Metal Conductivity. *Chem. Phys. Lett.* **1998**, *298*, 315–319.
16. Caruso, F.; Schuler, C. Enzyme Multilayers on Colloid Particles: Assembly, Stability, and Enzymatic Activity. *Langmuir* **2000**, *16*, 9595–9603.
17. He, J. A.; Valluzzi, R.; Yang, K.; Dolukhanyan, T.; Sung, C. M.; Kumar, J.; Tripathy, S. K.; Samuelson, L.; Balogh, L.; Tomalia, D. A. Electrostatic Multilayer Deposition of a Gold-Dendrimer Nanocomposite. *Chem. Mater.* **1999**, *11*, 3268–3274.
18. Wang, Y.; Angelatos, A. S.; Caruso, F. Template Synthesis of Nanostructured Materials via Layer-by-Layer Assembly. *Chem. Mater.* **2008**, *20*, 848–858.
19. Zhang, J.; Senger, B.; Vautier, D.; Picart, C.; Schaaf, P.; Voegel, J.-C.; Lavalle, P. Natural Polyelectrolyte Films Based on Layer-by-Layer Deposition of Collagen and Hyaluronic Acid. *Biomaterials* **2005**, *26*, 3353–3361.
20. Hillebrenner, H.; Buyukserin, F.; Kang, M.; Mota, M. O.; Stewart, J. D.; Martin, C. R. Corking Nano Test Tubes by Chemical Self-Assembly. *J. Am. Chem. Soc.* **2006**, *128*, 4236–4237.
21. Hoyer, P.; Masuda, H. Electrodeposited Nanoporous TiO<sub>2</sub> Film by a Two-Step Replication Process from Anodic Porous Alumina. *J. Mater. Sci. Lett.* **1996**, *15*, 1228–1230.
22. Kriha, O.; Zhao, L. L.; Pippel, E.; Gosele, U.; Wehrspohn, R. B.; Wendorff, J. H.; Steinhart, M.; Greiner, A. Organic Tube/Rod Hybrid Nanofibers with Adjustable Segment Lengths by Bidirectional Template Wetting. *Adv. Funct. Mat.* **2007**, *17*, 1327–1332.
23. Lei, Y.; Cai, W. P.; Wilde, G. Highly Ordered Nanostructures with Tunable Size, Shape, and Properties: A New Way to Surface Nano-Patterning Using Ultra-Thin Alumina Masks. *Prog. Mater Sci.* **2007**, *52*, 465–539.
24. Martin, C. R. Nanomaterials—A Membrane-Based Synthetic Approach. *Science* **1994**, *266*, 1961–1966.
25. Masuda, H.; Fukuda, K. Ordered Metal Nanohole Arrays Made by a 2-Step Replication of Honeycomb Structures of Anodic Alumina. *Science* **1995**, *268*, 1466–1468.
26. Mikulskas, I.; Juodkazis, S.; Tomasiunas, R.; Dumas, J. G. Aluminum Oxide Photonic Crystals Grown by a New Hybrid Method. *Adv. Mater.* **2001**, *13*, 1574–1577.
27. Schmid, G. Materials in Nanoporous Alumina. *J. Mater. Chem.* **2002**, *12*, 1231–1238.
28. Steinhart, M.; Wehrspohn, R. B.; Gosele, U.; Wendorff, J. H. Nanotubes by Template Wetting: A Modular Assembly System. *Angew. Chem., Int. Ed.* **2004**, *43*, 1334–1344.
29. O'Sullivan, J. P.; Wood, G. C. The Morphology and Mechanism of Formation of Porous Anodic Films on Aluminum. *Proc. R. Soc. London, A* **1970**, *317*, 511–543.
30. Nielsch, K.; Choi, J.; Schwirn, K.; Wehrspohn, R. B.; Gosele, U. Self-Ordering Regimes of Porous Alumina: The 10% Porosity Rule. *Nano Lett.* **2002**, *2*, 677–680.
31. Lee, S. B.; Mitchell, D. T.; Trofin, L.; Nevanen, T. K.; Soderlund, H.; Martin, C. R. Antibody-Based Bio-nanotube Membranes for Enantiomeric Drug Separations. *Science* **2002**, *296*, 2198–2200.
32. Mitchell, D. T.; Lee, S. B.; Trofin, L.; Li, N. C.; Nevanen, T. K.; Soderlund, H.; Martin, C. R. Smart Nanotubes for Bioseparations and Biocatalysis. *J. Am. Chem. Soc.* **2002**, *124*, 11864–11865.
33. Vlassiouk, I.; Krasnolobodtsev, A.; Smirnov, S.; Germann, M. "Direct" Detection and Separation of DNA Using Nanoporous Alumina Filters. *Langmuir* **2004**, *20*, 9913–9915.
34. Chiem, N. H.; Harrison, D. J. Microchip Systems for Immunoassay: An Integrated Immunoreactor with Electrophoretic Separation for Serum Theophylline Determination. *Clin. Chem.* **1998**, *44*, 591–598.
35. Figeys, D.; Pinto, D. Lab-on-a-Chip: A Revolution in Biological and Medical Sciences. *Anal. Chem.* **2000**, *72*, 330A–335A.
36. Stone, H. A.; Stroock, A. D.; Ajdari, A. Engineering Flows in Small Devices: Microfluidics Toward a Lab-on-a-Chip. *Ann. Rev. Fluid Mech.* **2004**, *36*, 381–411.
37. Wang, J. From DNA Biosensors to Gene Chips. *Nucleic Acids Res.* **2000**, *28*, 3011–3016.
38. Biesheuvel, P. M.; Stroo, P.; Barneveld, P. A. Effect of Protein Adsorption and Ionic Strength on the Equilibrium Partition Coefficient of Ionizable Macromolecules in Charged Nanopores. *J. Phys. Chem. B* **2004**, *108*, 17660–17665.
39. Bosman, A. W.; Janssen, H. M.; Meijer, E. W. About Dendrimers: Structure, Physical Properties, and Applications. *Chem. Rev.* **1999**, *99*, 1665–1688.
40. Caminade, A. M.; Majoral, J. P. Nanomaterials Based on Phosphorus Dendrimers. *Acc. Chem. Res.* **2004**, *37*, 341–348.
41. Frechet, J. M. J.; Tomalia, D. A. *Dendrimers and Other*

*Dendritic Polymers*; John Wiley & Sons: Chichester, UK, 2001.

42. Majoral, J. P.; Caminade, A. M. Dendrimers Containing Heteroatoms. *Chem. Rev.* **1999**, *99*, 845–880.
43. Yu, Y.; Feng, C.; Caminade, A.-M.; Majoral, J.-P.; Knoll, W. The Detection of DNA Hybridization on Phosphorus Dendrimer Multilayer Films by Surface Plasmon Field Enhanced-Fluorescence Spectroscopy. *Langmuir* **2009**, *25*, 13680–13684.
44. Hou, S.; Harrell, C. C.; Trofin, L.; Kohli, P.; Martin, C. R. Layer-by-Layer Nanotube Template Synthesis. *J. Am. Chem. Soc.* **2004**, *126*, 5674–5675.
45. Kim, B. S.; Lebedeva, O. V.; Kim, D. H.; Caminade, A. M.; Majoral, J. P.; Knoll, W.; Vinogradova, O. I. Assembly and Mechanical Properties of Phosphorus Dendrimer/Polyelectrolyte Multilayer Microcapsules. *Langmuir* **2005**, *21*, 7200–7206.
46. Launay, N.; Caminade, A. M.; Lahana, R.; Majoral, J. P. A General Synthetic Strategy for Neutral Phosphorus-Containing Dendrimers. *Angew. Chem., Int. Ed.* **1994**, *33*, 1589–1592.
47. Adler, P. M. Influence of Colloidal Forces on a Closely-Fitting Sphere in a Fluid-Filled Tube. *Physicochem. Hydrodyn.* **1983**, *4*, 1–10.
48. Bhattacharjee, S.; Sharma, A. Apolar, Polar, and Electrostatic Interactions of Spherical Particles in Cylindrical Pores. *J. Colloid Interface Sci.* **1997**, *187*, 83–95.
49. Deen, W. M. Hindered Transport of Large Molecules in Liquid-Filled Pores. *AIChE J.* **1987**, *33*, 1409–1425.
50. Deen, W. M.; Bohrer, M. P.; Epstein, N. B. Effects of Molecular-Size and Configuration on Diffusion in Microporous Membranes. *AIChE J.* **1981**, *27*, 952–959.
51. Papadopoulos, K. D.; Kuo, C. C. The van der Waals Interaction between a Colloid and its Host Pore. *Colloids Surf.* **1990**, *46*, 115–125.
52. Pujar, N. S.; Zydny, A. L. Charge Regulation and Electrostatic Interactions for a Spherical Particle in a Cylindrical Pore. *J. Colloid Interface Sci.* **1997**, *192*, 338–349.
53. Smith, F. G.; Deen, W. M. Electrostatic Double-Layer Interactions for Spherical Colloids in Cylindrical Pores. *J. Colloid Interface Sci.* **1980**, *78*, 444–465.
54. Han, J. Y.; Fu, J. P.; Schoch, R. B. Molecular Sieving Using Nanofilters: Past, Present and Future. *Lab Chip* **2008**, *8*, 23–33.
55. Jiang, X. Q.; Mishra, N.; Turner, J. N.; Spencer, M. G. Diffusivity of Sub-1000 Da Molecules in 40 nm Silicon-Based Alumina Pores. *Microfluid. Nanofluid.* **2008**, *5*, 695–701.
56. Keh, H. J.; Chiou, J. Y. Electrophoresis of a Colloidal Sphere in a Circular Cylindrical Pore. *AIChE J.* **1996**, *42*, 1397–1406.
57. Smith, F. G.; Deen, W. M. Electrostatic Effects on the Partitioning of Spherical Colloids between Dilute Bulk Solution and Cylindrical Pores. *J. Colloid Interface Sci.* **1983**, *91*, 571–590.
58. Causserand, C.; Lafaille, J. P.; Aimar, P. Transmission of Biomolecules through Porous Membranes Triggered by an External Electric-Field. *J. Controlled Release* **1994**, *29*, 113–123.
59. Deen, W. M.; Smith, F. G. Hindered Diffusion of Synthetic Polyelectrolytes in Charged Microporous Membranes. *J. Membr. Sci.* **1982**, *12*, 217–237.
60. Verbrugge, M. W.; Schneider, E. W.; Conell, R. S.; Hill, R. F. The Effect of Temperature on the Equilibrium and Transport-Properties of Saturated Poly(perfluorosulfonic acid) Membranes. *J. Electrochem. Soc.* **1992**, *139*, 3421–3428.
61. Wong, C. T. A.; Muthukumar, M. Polymer Capture by Electro-osmotic Flow of Oppositely Charged Nanopores. *J. Chem. Phys.* **2007**, *126*, 164903.
62. Bezrukov, S. M.; Vodyanoy, I.; Parsegian, V. A. Counting Polymers Moving through a Single-Ion Channel. *Nature* **1994**, *370*, 279–281.
63. Chang, H.; Kosari, F.; Andreadakis, G.; Alam, M. A.; Vasmatzis, G.; Bashir, R. DNA-Mediated Fluctuations in Ionic Current through Silicon Oxide Nanopore Channels. *Nano Lett.* **2004**, *4*, 1551–1556.
64. Saleh, O. A.; Sohn, L. L. Quantitative Sensing of Nanoscale Colloids Using a Microchip Coulter Counter. *Rev. Sci. Instrum.* **2001**, *72*, 4449–4451.
65. Roy, C. J.; Dupont-Gillain, C.; Demoustier-Champagne, S.; Jonas, A. M.; Landoulsi, J. Growth Mechanism of Confined Polyelectrolyte Multilayers in Nanoporous Templates. *Langmuir* **2010**, *26*, 3350–3355.
66. Knoll, W. Interfaces and Thin Films as Seen by Bound Electromagnetic Waves. *Annu. Rev. Phys. Chem.* **1998**, *49*, 569–634.
67. Dürr, M.; Menges, G.; Knoll, W.; Yasuda, A.; Nelles, G. Direct Measurement of Increased Light Intensity in Optical Waveguides Coupled to a Surface Plasmon Spectroscopy Setup. *App. Phys. Lett.* **2007**, *91*, 021113–021115.
68. Lau, K. H. A.; Tan, L. S.; Tamada, K.; Sander, M. S.; Knoll, W. Highly Sensitive Detection of Processes Occurring Inside Nanoporous Anodic Alumina Templates: A Waveguide Optical Study. *J. Phys. Chem. B* **2004**, *108*, 10812–10818.
69. Lau, K. H. A.; Cameron, P. J.; Duran, H.; Abou-Kandil, A. I.; Knoll, W. Nanoporous Thin Films as Highly Versatile and Sensitive Waveguide Biosensors. In *Surface Design: Applications in Bioscience and Nanotechnology*; Förch, R., Schönherr, H., Jenkins, A. T. A., Eds.; Wiley-VCH Verlag: Weinheim, Germany, 2009; pp 383–401.
70. Lau, K. H. A.; Duran, H.; Knoll, W. *In Situ* Characterization of N-carboxy Anhydride Polymerization in Nanoporous Anodic Alumina. *J. Phys. Chem. B* **2009**, *113*, 3179–3189.
71. Cameron, P. J.; Jenkins, A. T. A.; Knoll, W.; Marken, F.; Milsom, E. V.; Williams, T. L. Optical Waveguide Spectroscopy Study of the Transport and Binding of Cytochrome c in Mesoporous Titanium Dioxide Electrodes. *J. Mater. Chem.* **2008**, *18*, 4304–4310.
72. Awazu, K.; Rockstuhl, C.; Fujimaki, M.; Fukuda, N.; Tominaga, J.; Komatsubara, T.; Ikeda, T.; Ohki, Y. High Sensitivity Sensors Made of Perforated Waveguides. *Opt. Express* **2007**, *15*, 2592–2597.
73. Fujimaki, M.; Rockstuhl, C.; Wang, X. M.; Awazu, K.; Tominaga, J.; Koganezawa, Y.; Ohki, Y.; Komatsubara, T. Silica-Based Monolithic Sensing Plates for Waveguide-Mode Sensors. *Opt. Express* **2008**, *16*, 6408–6416.
74. Reimhult, E.; Kumar, K.; Knoll, W. Fabrication of Nanoporous Silicon Nitride and Silicon Oxide Films of Controlled Size and Porosity for Combined Electrochemical and Waveguide Measurements. *Nanotechnology* **2007**, *18*, 275303.
75. Kim, D. H.; Lau, K. H. A.; Joo, W.; Peng, J.; Jeong, U.; Hawker, C. J.; Kim, J. K.; Russell, T. P.; Knoll, W. An Optical Waveguide Study on the Nanopore Formation in Block Copolymer/Homopolymer Thin Films by Selective Solvent Swelling. *J. Phys. Chem. B* **2006**, *110*, 15381–15388.
76. Egan, W. G.; Aspnes, D. E. Finite-Wavelength Effects in Composite Media. *Thin Solid Films* **1982**, *89*, 249–262.
77. Foss, C. A.; Tierney, M. J.; Martin, C. R. Template Synthesis of Infrared-Transparent Metal Microcylinders: Comparison of Optical Properties with the Predictions of Effective Medium Theory. *J. Phys. Chem.* **1992**, *96*, 9001–9007.
78. Schmid, G.; Emmrich, E.; Majoral, J.-P.; Caminade, A.-M. The Behavior of Au55 Nanoclusters on and in Thiol-Terminated Dendrimer Monolayers. *Small* **2005**, *1*, 73–75.
79. Emmrich, E.; Franzka, S.; Schmid, G.; Majoral, J.-P. Monolayers of a Fourth-Generation Thiol-Terminated Dendrimer. *Nano Lett.* **2002**, *2*, 1239–1242.
80. Leclaire, J.; Coppel, Y.; Caminade, A.-M.; Majoral, J.-P. Nanometric Sponges Made of Water-Soluble Hydrophobic Dendrimers. *J. Am. Chem. Soc.* **2004**, *126*, 2304–2305.
81. Lazzara, T. D.; Lau, K. H. A.; Knoll, W. Mounted Nanoporous Anodic Alumina Thin Films as Planar Optical Waveguides. *J. Nanosci. Nanotechnol.* **2010**, *10*, 4293–4299.
82. Choy, T. C. *Effective Medium Theory: Principles and Applications*, 1st ed.; Oxford University Press: New York, 1999; Vol. 102.
83. The agreement with the deposition atop the AAO

membranes with  $D_0 = 97$  nm was looser. This can likely be attributed to the modifications in AAO preparation conditions in order to produce membranes with such large pores (see Experimental section), which also produced a wider spread in the distributions of pore diameters and average center-to-center distance ( $\lambda_{c.c.}$ ) between pores.

84. Glinel, K.; Moussa, A.; Jonas, A. M.; Laschewsky, A. Influence of Polyelectrolyte Charge Density on the Formation of Multilayers of Strong Polyelectrolytes at Low Ionic Strength. *Langmuir* **2002**, *18*, 1408–1412.
85. Borisov, O. V.; Zhulina, E. B. Effects of Ionic Strength and Charge Annealing in Star-Branched Polyelectrolytes. *Eur. Phys. J. B* **1998**, *4*, 205–217.
86. Steitz, R.; Jaeger, W.; Klitzing, R. Influence of Charge Density and Ionic Strength on the Multilayer Formation of Strong Polyelectrolytes. *Langmuir* **2001**, *17*, 4471–4474.
87. Bruening, M. L.; Dotzauer, D. M.; Jain, P.; Ouyang, L.; Baker, G. L. Creation of Functional Membranes Using Polyelectrolyte Multilayers and Polymer Brushes. *Langmuir* **2008**, *24*, 7663–7673.
88. Loup, C.; Zanta, M. A.; Caminade, A. M.; Majoral, J. P.; Meunier, B. Preparation of Water-Soluble Cationic Phosphorus-Containing Dendrimers as DNA Transferring Agents. *Chem.—Eur. J.* **1999**, *5*, 3644–3650.
89. Raether, H. *Surface-Plasmons on Smooth and Rough Surfaces and on Gratings*; Springer: Berlin/Heidelberg, 1988; Vol. 111.
90. Talbot, J.; Tarjus, G.; Van Tassel, P. R.; Viot, P. From Car Parking to Protein Adsorption: An Overview of Sequential Adsorption Processes. *Colloids Surf., A* **2000**, *165*, 287–324.